Journal of
Materials Chemistry A

ROYAL SOCIETY
OF CHEMISTRY

PAPER

View Article Online
View Journal | View Issue

Cite this: *J. Mater. Chem. A*, 2023, **11**, 24738

Tailoring the shell thickness of yolk–shell structured carbon microspheres: applications in metal selenide and carbon composite microspheres for enhanced sodium ion storage properties†

Hyo Yeong Seo,‡[a] Jae Hyeon Choi,‡[a] Yeong Beom Kim,[ac] Jung Sang Cho, *[b] Yun Chan Kang *[c] and Gi Dae Park *[a]

Received 7th August 2023
Accepted 26th October 2023

DOI: 10.1039/d3ta04705a

rsc.li/materials-a

The yolk–shell structured material, characterized by its core@void@shell configuration, has garnered considerable attention as an anode material for sodium ion batteries due to its advantageous internal void space, large surface area, and short ion diffusion distance. While previous studies have mainly focused on controlling the thickness of the outer shell in a yolk@void@pure carbon shell configuration, tailoring the optimized thickness of the outer shell in metal compounds–carbon composites has not been reported until now. In this study, we propose a novel strategy for tailoring the thickness of the outer shell in yolk–shell structured carbon microspheres using spray pyrolysis. These carbon microspheres possess abundant pores and offer variable outer shell thickness, making them an ideal reservoir for nickel–cobalt selenide composites. Through optimization of the yolk–shell structured nickel–cobalt selenide–carbon composites for sodium ion batteries (SIBs), we achieved exceptional electrochemical performance, capitalizing on their structural advantages. The optimized nickel–cobalt selenide–carbon yolk–shell composite microspheres exhibited a remarkable cycling lifetime, retaining 344 mA h g^{-1} over 200 cycles at 0.5 A g^{-1}, as well as an excellent rate capability, delivering 237 mA h g^{-1} at 5 A g^{-1}.

1. Introduction

Over the past few decades, the yolk–shell structure has emerged as a novel class of core/shell configurations, featuring a distinct core@void@shell arrangement, and has garnered significant interest as a potential anode material for sodium ion batteries (SIBs).[1–6] Yolk–shell structures offer two distinct spaces, namely the yolk and shell, to compose a particle, resulting in a unique interior void space, large surface area, and short ion diffusion distance.[7–9] These structural advantages effectively address the challenges of volume expansion and aggregation commonly encountered with anode materials in SIBs. Given the importance of structural strength, numerous synthesis approaches have been explored to prepare yolk–shell structures. These strategies include selective etching, templating assembly, carbon combustion, Ostwald ripening, galvanic replacement, and the Kirkendall effect, among others, and have contributed to the growing commercial interest in yolk–shell structured materials.[10–15]

When considering yolk–shell structures as anode materials from a structural standpoint, outer shells play a dual role by providing structural robustness and preventing agglomeration of active materials, thereby maintaining the stability of SEI (solid electrolyte interphase) layers.[16,17] In particular, when the outer shell is made of pure carbon or a composite of metal compound nanocrystals, it enhances both electrical conductivity and structural flexibility. Despite the progress in synthetic methods for yolk–shell structures, the control of outer shell thickness has primarily been reported for yolk@void@pure carbon shell configurations. For instance, Zhang *et al.* reported the synthesis of yolk–shell structured Sn@C nanoboxes with tunable carbon shell thickness through carbon coating and selective etching processes, showing that the shell thickness significantly influences both nanostructures and electrochemical performance.[18] Similarly, Wang *et al.* demonstrated the tailoring of carbon shell thickness in SnCo@nitrogen-doped

---

[a] *Department of Advanced Materials Engineering, Chungbuk National University, Chungdae-ro 1, Seowon-Gu, Cheongju, Chungbuk 28644, Republic of Korea. E-mail: gdpark@chungbuk.ac.kr; Fax: +82-43-271-3222*

[b] *Department of Engineering Chemistry, Chungbuk National University, Chungdae-ro 1, Seowon-Gu, Cheongju, Chungbuk 28644, Republic of Korea. E-mail: jscho@cbnu.ac.kr; Fax: +82-43-262-2380*

[c] *Department of Materials Science and Engineering, Korea University, Anam-Dong, Seongbuk-Gu, Seoul 136-713, Republic of Korea. E-mail: yckang@korea.ac.kr; Fax: +82-2-928-3584*

† Electronic supplementary information (ESI) available. See DOI: https://doi.org/10.1039/d3ta04705a

‡ These authors contributed equally to this work.

carbon nanocages for lithium storage. They coated the prepared hollow nanocubes with a polydopamine carbon component through co-precipitation and alkaline etching, and the optimized carbon shell thickness resulted in remarkably improved cycling stability.[19] Interestingly, to the best of our knowledge, there have been no reports on tailoring the optimized thickness of the outer shell composed of a metal compounds–carbon composite. This presents an exciting and unexplored avenue for future research in the field of yolk–shell structures as anode materials.

Metal selenides, as conversion/alloying-based anode materials for sodium ion storage, have been extensively researched due to their high theoretical capacities. However, they face challenges related to severe volume changes during cycling, resulting in kinetic issues and poor electrochemical stability.[20–25] To address these problems in sodium ion batteries (SIBs), the use of yolk–shell structured metal selenide and carbon composites has emerged as a promising solution. Recently, several studies have focused on fabricating yolk–shell structured metal selenide@void@C materials through routes involving metal–organic frameworks (MOFs) *via* Ostwald ripening and anion exchange strategies.[26–29] Additionally, diverse approaches, such as metal salt infiltration into hollow carbon nanospheres, have been employed for the synthesis of yolk–shell structured metal selenide–C composites.[30–32] From a structural perspective, it is crucial to investigate the optimized thickness of the outer shell to ensure the efficient diffusion of sodium ions into the structure while maintaining its structural stability. Notably, anode materials for sodium ion batteries experience a larger volume change compared to those used in lithium-ion batteries, making the process of optimizing the structure even more critical.[33–37]

Recently, novel strategies have been proposed for synthesizing nanostructured metal compound–carbon composites by infiltrating metal salts into specifically designed carbon materials, presenting promising new synthetic methods for anode materials. In this study, we introduce a pioneering approach to optimize the shell thickness of yolk–shell structured metal selenide and carbon composites. For the first time, a method has been devised to synthesize carbon materials with an adjustable shell thickness. In the yolk@void@carbon shell configuration, we successfully controlled the outer carbon shell, enabling precise tailoring of the shell thickness for the yolk–shell structured metal selenide and carbon composite. Our study involved the successful fabrication of yolk–shell structured nickel–cobalt selenide–carbon composite microspheres, and through comprehensive morphological and electrochemical analysis, we systematically determined the optimized outer shell thickness.

2. Experimental section

Yolk–shell structured carbon microspheres, allowing for the tailoring of shell thickness, were prepared using spray pyrolysis, selenization, and etching processes. In the spray pyrolysis step, droplets were generated using a 1.7 MHz ultrasonic spray generator with six vibrators. The droplets were carried to a quartz reactor (1200 mm length, 50 mm diameter) maintained at 400 °C, using air as the carrier gas at a flow rate of 10 L min^{-1}. The spray solution was prepared by dissolving 0.2 M of tin(II) oxalate, 0.2 M of magnesium nitrate hexahydrate, 0.05 M of sucrose, and a certain concentration of PVP ($M_w = 40\,000$) in 1 L of distilled water. The spray solution contained various ratios of sucrose and PVP, specifically 0/1, 1/1, 2/1, 4/1, and 16/1 wt%. After spray pyrolysis of these solutions, SnO_x–MgO–C@C microspheres are obtained. These precursor powders were post-treated in a tube furnace at 1000 °C under a 10% H_2/Ar atmosphere for 3 h. This treatment transformed SnO_x–MgO–C@C into MgO–MgSe–C@C microspheres. During selenization, the SnO_x–MgO–C@C microspheres first changed into SnSe–MgO–MgSe–C@C microspheres. Then, at 1000 °C, the SnSe component evaporated, resulting in MgO–MgSe–C@C microspheres. Subsequently, the obtained MgO–MgSe–C@C microspheres were etched using an HCl/HNO_3 solution to produce yolk–shell structured carbon microspheres. For the preparation of nickel–cobalt selenide–yolk–shell composite microspheres, carbon yolk–shell microsphere powders were mixed with a solution containing nickel nitrate hexahydrate ($Ni(NO_3)_2 \cdot 6H_2O$) and cobalt nitrate hexahydrate ($Co(NO_3)_2 \cdot 6H_2O$) dissolved in high-purity ethyl alcohol. In this research, to express the molar ratio of nickel and cobalt, nickel : cobalt $= x : y$ is expressed as NC($x : y$). NC(1 : 1)Se–C-YS was prepared by infiltration of solution dissolved with 1.75 g of nickel nitrate and 1.75 g of cobalt nitrate into 1 g of carbon yolk–shell microsphere. NC(1 : 0)Se–C-YS 2/1 was prepared by infiltration of solution dissolved with 3.5 g of nickel nitrate into 1 g of carbon yolk–shell microsphere powders. NC(2 : 1)Se–C-YS 2/1 was prepared by infiltration of solution dissolved with 2.33 g of nickel nitrate and 1.17 g of cobalt nitrate into 1 g of carbon yolk–shell microsphere powders. NC(1 : 2)Se–C-YS 2/1 was prepared by infiltration of solution dissolved with 1.17 g of nickel nitrate and 2.33 g of cobalt nitrate into 1 g of carbon yolk–shell microsphere powders. NC(0 : 1)Se–C-YS 2/1 was prepared by infiltration of solution dissolved with 3.5 g of cobalt nitrate into 1 g of carbon yolk–shell microsphere powders. The infiltrated powders were then uniformly mixed with selenium nanopowders and subjected to selenization at 260 °C for 12 hours and 300 °C for 6 hours under a 10% H_2/Ar atmosphere to form nickel–cobalt selenide–carbon yolk–shell composite microspheres. For detailed information regarding the characterization and electrochemical measurements of the prepared samples, please refer to the ESI.†

3. Results and discussion

The new formation mechanism, allowing the tailoring of the shell thickness in yolk–shell structured carbon microspheres, is illustrated in Scheme 1. To produce the yolk–shell carbon microspheres, sucrose and polyvinylpyrrolidone (PVP) served as key components for forming the yolk and shell parts, respectively. To demonstrate the role of PVP in the formation process, droplets containing tin oxalate, magnesium nitrate, and sucrose (without PVP) were pyrolyzed, leading to the formation of SnO_x–MgO–C composite precursor microspheres (Scheme 1a).

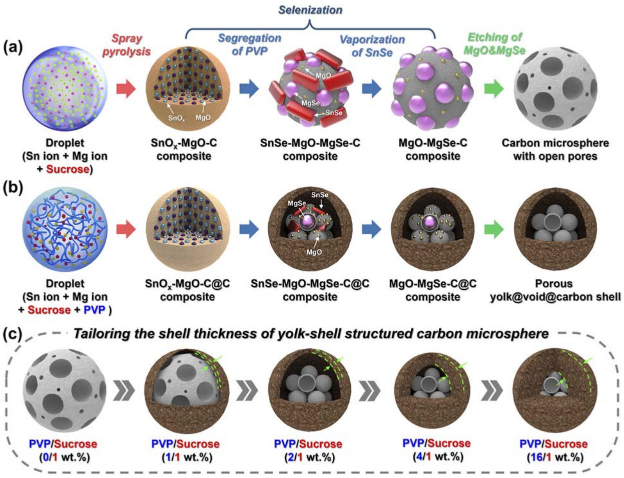

Scheme 1 Schematic illustration of the formation mechanism for (a) carbon microsphere with open pores and (b) porous yolk@void@carbon shell and (c) the variation in shell thickness as the ratio of PVP/sucrose.

Subsequent selenization of the precursor resulted in the evaporation of SnSe and transformation into MgO–MgSe–C microspheres at 1000 °C. Acid etching then removed the MgO–MgSe component, creating porous carbon microspheres with a well-defined open pore structure. This removal process led to the formation of macro- and mesopores in the carbon microspheres. In contrast, under the same synthetic conditions, droplets containing tin oxalate, magnesium nitrate, sucrose, and PVP were pyrolyzed, forming SnO_x–MgO–C@C microspheres (Scheme 1b). During pyrolysis, PVP tended to be pushed out of the particles, while sucrose effectively composited with metal oxide crystals inside the particles. This compositional difference was the key factor responsible for the formation of yolk–shell structured carbon microspheres. Following the same post-treatment steps involving selenization and etching, the resulting structure exhibited a porous carbon yolk@void@shell configuration. Interestingly, the yolk part exhibited morphologies resembling hollow nanosphere aggregates, attributed to the etching of MgO–MgSe nanocrystals, except for the sucrose-derived carbon shell surrounding these nanocrystals. As demonstrated by the role of PVP sources, the thickness of the carbon shell could be freely adjusted based on the amount of PVP added to the spray solution (Scheme 1c).

To illustrate the role of PVP sources in tailoring the shell thickness of yolk–shell structured carbon microspheres, we present the morphological characteristics of the sprayed precursor, selenized intermediate products, and final pure carbon microspheres prepared with varying amounts of PVP (Fig. 1 and S1†). The low-magnified SEM images in Fig. S1a–e† reveal spherical microspheres regardless of the amount of PVP, with some variation in particle sizes. This is attributed to each microsphere being formed from one droplet generated by the ultrasonic spray generator. The high-magnified SEM images in Fig. 1a–e provide more detailed views of individual microspheres according to the amount of PVP. Although the microspheres initially appear to have a completely filled structure, the boundary between the yolk and shell becomes clearer as the amount of PVP increases, as indicated by the arrows in Fig. 1a–e. The XRD pattern in Fig. S2† shows that the sprayed precursor exhibits an amorphous state due to the short residence time of decomposed immediate microspheres from droplets, caused by the rapid carrier gas flow rate during spray pyrolysis. After the selenization process of the sprayed precursor, SEM images in Fig. 1f–j reveal the presence of MgO–MgSe nanocrystals, with variations according to the amount of PVP, as confirmed by the XRD pattern in Fig. S2.† Interestingly, in the absence of PVP (Fig. 1f and S1f†), the shell encapsulating nanocrystals is not observed. The low-magnified SEM images in Fig. S1g–j† show spherical microspheres overall, but broken microspheres in Fig. 1g–j clearly demonstrate that the shell thickness increases as the amount of PVP increases. The shell formed from PVP effectively surrounds the nanocrystals. Finally, pure carbon microspheres were successfully obtained through the acid etching process, as verified by the XRD pattern in Fig. S2.† The SEM image in Fig. 1k displays spherical shapes with large voids on the surface and inner space, indicating that some nanocrystals are pushed out of the carbon derived from sucrose, while others are complexed with carbon. In contrast, the samples with added PVP are well wrapped in the carbon shell, forming the yolk–shell structure. As expected, the selenized samples confirm that the carbon shell thickness increases with the increase in the amount of PVP, as shown in Fig. 1l–o.

To gain a more visual understanding of the interior of the carbon structures, pure carbon nanostructures synthesized under representative conditions with different ratios of PVP/sucrose (0/1, 2/1, and 16/1 wt%) were observed through TEM analysis, as shown in Fig. 2. Each carbon microsphere, prepared under specific conditions (PVP/sucrose ratios), was denoted as C-YS 0/1, C-YS 2/1, and C-YS 16/1, respectively. The SEM images in Fig. 1k confirmed that C-YS 0/1, synthesized without PVP and using only sucrose, displayed an open-pore structure with meso and macropore sizes, as shown in Fig. 2a and b. Additionally, the high-magnification TEM image in Fig. 2c revealed mesopores on the surface shell. Elemental mapping images in Fig. 2d demonstrated the complete elimination of SnSe and MgO–MgSe components during the acid etching process, resulting in pure carbon microspheres. The pure carbon microspheres prepared under conditions of spray solutions with ratios of PVP/sucrose (2/1 and 16/1 wt%) clearly exhibited the yolk (hollow nanospheres-aggregates)@void@shell configuration, as shown in Fig. 2e, f, i and j. Comparing the carbon yolk–shell microspheres prepared from spray solutions with ratios of PVP/sucrose (2/1, 16/1 wt%), it was evident that the thickness of the outermost carbon shell significantly increased as the amount of PVP in the spray solution increased, ranging from 45.18 to 176.25 nm, as shown in Fig. 2g and k. This suggests that PVP was pushed outward to form a shell during the pyrolysis step. Moreover, it became apparent that the simultaneous utilization of PVP and sucrose was necessary for the formation of the yolk–shell structure. The elemental mapping images in Fig. 2h and l consistently demonstrated the complete etching of other metal compounds, resulting in the formation of pure carbon microspheres. To further characterize the specific

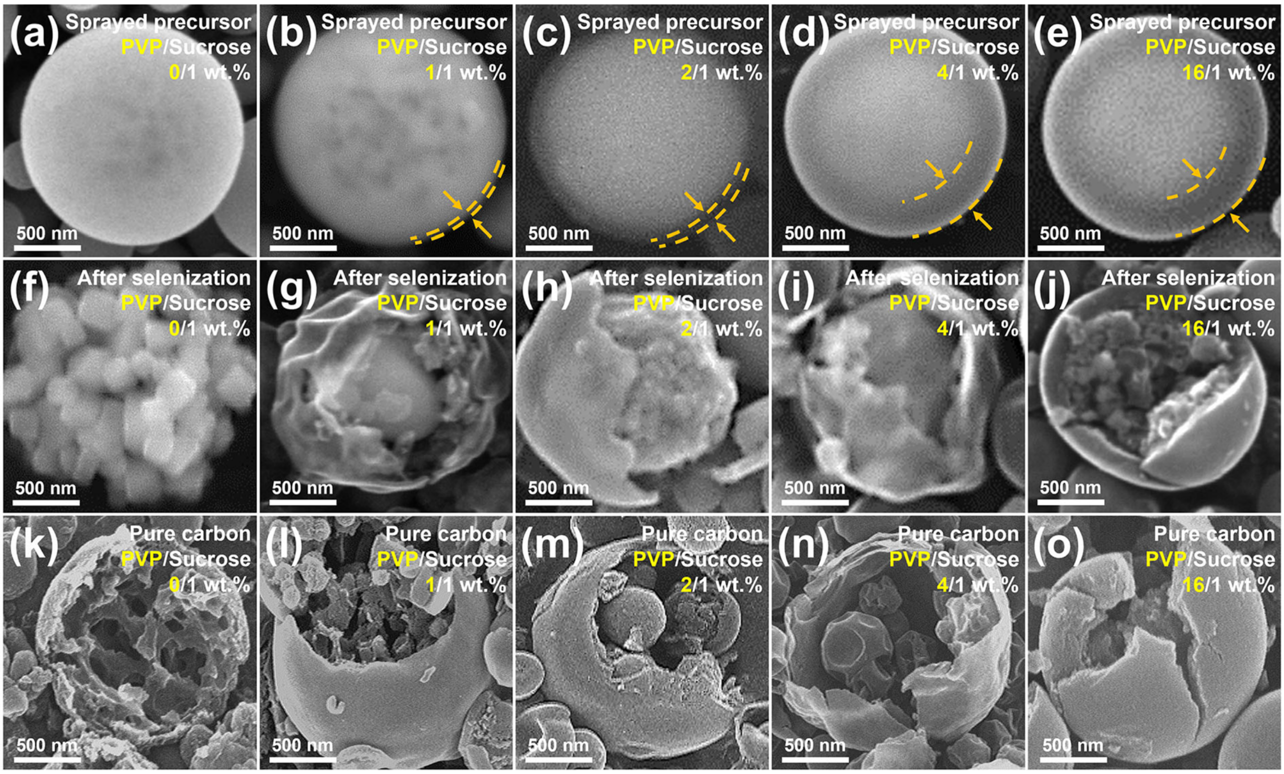

Fig. 1 Morphological characteristics of SEM images of (a–e) SnO_x–MgO–C@C composite precursors prepared from the spray solution containing Sn oxalate, Mg nitrate, sucrose, and PVP with different ratios of PVP/sucrose, (f–j) SnSe–MgO–MgSe–C@C obtained after selenization of the precursor, and (k–o) carbon yolk–shell obtained after the etching process: (a, f and k) PVP/sucrose 0/1 wt%, (b, g and l) PVP/sucrose 1/1 wt%, (c, h and m) PVP/sucrose 2/1 wt%, (d, i and n) PVP/sucrose 4/1 wt%, and (e, j and o) PVP/sucrose 16/1 wt%.

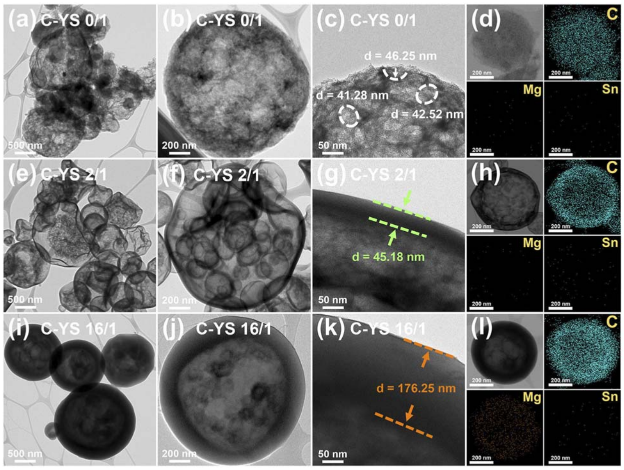

Fig. 2 TEM images and elemental mapping images of (a–d) C-YS 0/1, (e–h) C-YS 2/1, and (i–l) C-YS 16/1: (a, b, e, f, i and j) TEM images, (c, g and k) HR-TEM images and (d, h and l) elemental mapping images.

surface area and pore structure of the various samples, where the shell thickness of yolk–shell structured carbon microspheres was controlled based on the amount of PVP, Brunauer–Emmett–Teller (BET) and Barrett–Joyner–Halenda (BJH) measurements were conducted, as shown in Fig. S3.† From C-YS 0/1 with no PVP to C-YS 16/1 with gradually added PVP, isotherms commonly exhibited type IV with an H3 hysteresis loop, indicating the presence of micro- and mesopores in the carbon yolk and shell, and some macropores in the void of the yolk–shell structure. The BET surface areas of the carbon yolk–shell microspheres with different ratios of PVP/sucrose in spray solution (0/1, 1/1, 2/1, 4/1, and 16/1 wt%) were 720, 1074, 1228, 1330, and 858 m^2 g^{-1}. Moreover, it was observed that as the amount of PVP increased, the specific surface area also increased, accompanied by variations in the pore size distribution, as shown in Fig. S3.† For instance, C-YS 1/1 showed ~10 nm pores, which gradually developed towards C-YS 4/1 conditions where PVP was gradually added. C-YS 2/1, as an intermediate condition, generally exhibited pore development in the range of 10 to 20 nm. Interestingly, in C-YS 16/1, with excessive PVP, it was evident that 10–20 nm pores were hardly developed. This suggests that, with the same amount of sucrose, changes in the pore structure occurred during the formation of the shell, according to the amount of PVP added.

In this study, we successfully synthesized yolk–shell structured carbon microspheres with controlled shell thickness by varying the amount of PVP. The resulting microspheres exhibited abundant micro and mesopores, as confirmed by BET analysis, making them suitable as storage reservoirs for impregnating metal salts. The formation mechanism for the synthesis of metal selenide–carbon composite yolk–shell microspheres is described in Scheme 2. A solution containing various transition metal salts was impregnated into the carbon microspheres using a simple drop and dry method. Subsequently, selenization was carried out in the presence of selenium powders, transforming the metal salts into metal selenides. During the selenization process, the molten selenium infiltrated into the small pores of the metal salt-infiltrated carbon yolk–shell microspheres, leading to the formation of metal selenide nanocrystals within the carbon yolk–shell microspheres. As a specific example, we applied the nickel–cobalt binary metal selenide and carbon composite yolk–shell microspheres, denoted as NC(1 : 1)Se–C-YS, as our target material in this research.

The morphological characteristics of NC(1 : 1)Se–C-YS, depending on the ratio of PVP/sucrose, are presented in Fig. S4.† The NC(1 : 1)Se–C-YS sample prepared without PVP and only using sucrose (denoted as NC(1 : 1)Se–C-YS 0/1) exhibited nickel–cobalt selenide nanocrystals growing out of the carbon microsphere due to the Ostwald ripening effect. The absence of an outer shell and the open pore structure further accelerated this effect (Fig. S4a and b†). On the other hand, with the addition of PVP, the surface of the microspheres exhibited a crumpled appearance at low PVP content, but as the amount of PVP increased, a smooth spherical shape was clearly observed. This was due to the formation of a PVP-derived carbon outer shell (Fig. S4c–j†). NC(1 : 1)Se–C-YS 1/1 and NC(1 : 1)Se–C-YS 2/1 samples showed similar morphologies. To gain a clearer view of the yolk–shell structure inside the particle with different interior structures, TEM analysis was performed on the NC(1 : 1)Se–C-YS 1/1, NC(1 : 1)Se–C-YS 2/1, NC(1 : 1)Se–C-YS 4/1, and NC(1 : 1)Se–C-YS 16/1 samples, and the results are shown in Fig. 3. The low-magnified TEM images showed an increasing shell thickness from NC(1 : 1)Se–C-YS 1/1 to NC(1 : 1)Se–C-YS 16/1. For NC(1 : 1)Se–C-YS 1/1, the distinction between shell and yolk wasn't clear. As the amount of PVP further increased in the cases of NC(1 : 1)Se–C-YS 4/1 and NC(1 : 1)Se–C-YS 16/1, nanocrystals were observed in the outermost shell, and an excessive amount of nanocrystals were observed in the case of NC(1 : 1)Se–C-YS 16/1. The SEM images in Fig. S4† provide a complementary visual perspective. According to the BET analysis, it is evident that in the cases of C-YS 4/1 and 16/1, where 10 nm mesopores were not developed, the impregnation of the solution inside the C-YS microspheres was not as smooth, leading to the nanocrystals growing predominantly on the outside of the particle. Interestingly, NC(1 : 1)Se–C-YS 2/1 samples distinctly revealed the formation of yolk–shell structured microspheres, with ultrafine nanocrystals observed in the yolk and shell regions, respectively. This observation confirmed that the solution containing nickel and cobalt ions successfully infiltrated into the highly porous carbon yolk–shell microspheres. The high-resolution TEM images of NC(1 : 1)Se–C-YS 1/1, NC(1 : 1)Se–C-YS 2/1, and NC(1 : 1)Se–C-YS 4/1 showed that the nickel and cobalt selenide nanocrystals were well distributed over the yolk–shell structure, with clear lattice fringes separated by 0.20 and 0.18 nm, corresponding to the (102) and (110) crystal planes of NiSe and CoSe phases respectively. The selected-area electron diffraction (SAED) patterns also confirmed the formation of NiSe and CoSe phases, indicating that the NC(1 : 1)Se–C-YS 2/1 samples consisted of a $(Ni_{0.5}Co_{0.5})Se$ solid-solution (Fig. S5†). Moreover, the HR-TEM images of NC(1 : 1)Se–C-YS 16/1 show clear lattice fringes separated by 0.20 nm and 0.18 nm, corresponding to the (102) and (440) crystal planes of $Ni_{0.85}Se$ and Co_9Se_8 phases respectively. The elemental mapping images of the four samples clearly showed the formation of the nickel–cobalt selenide–C-composite, with the N mapping image indicating the presence of a PVP-derived N-doped carbon component (Fig. S6†). NC(1 : 1)Se–C-YS 2/1, as verified by the EDS data in Fig. S7 and Table S1,† has a molar ratio of 1 : 1 between $NiSe_x$ and $CoSe_x$. Within this compound, the weight percentages of Ni, Co, and Se are 7.99 wt%, 7.91 wt%, and 24.2 wt%, respectively. Converted to atomic percentages, the contents of Ni, Co, and Se are 0.14 at%, 0.13 at%, and 0.30 at%, respectively.

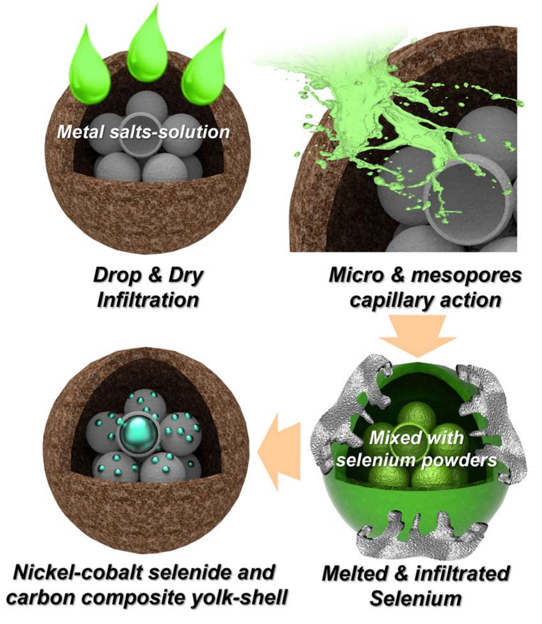

Scheme 2 Schematic illustration of the formation of nickel–cobalt selenide embedded in carbon yolk–shell 2/1.

The crystal structures of NC(1 : 1)Se–C-YS, varying with the amount of PVP, were analyzed by X-ray diffraction (XRD) as shown in Fig. 4a. From NC(1 : 1)Se–C-YS 1/1 to NC(1 : 1)Se–C-YS 16/1, it was observed that different phases were formed depending on the amount of PVP. In the cases of NC(1 : 1)Se–C-YS 1/1 and 2/1 with a small amount of PVP, the $(Ni_{0.5}Co_{0.5})Se$ phase was dominant, and as the PVP content gradually increased, the $Ni_{0.85}Se$ and Co_9Se_8 phases coexisted in NC(1 : 1)Se–C-YS 4/1 and NC(1 : 1)Se–C-YS 16/1. To observe the chemical state of NC(1 : 1)Se–C-YS 2/1 specifically, X-ray photoelectron spectroscopy (XPS) analysis was carried out, and the results are shown in Fig. 4b–f and S8.† The survey spectrum of NC(1 : 1)Se–C-YS 2/1 in Fig. S8† displayed peaks attributed to Ni, Co, Se, O, N, and C. The O elements were derived from unavoidable surface adsorption of the sample exposed to air. The Ni 2p spectrum in Fig. 4b exhibited $Ni_{3/2}$ and $Ni_{1/2}$ peaks at 852.9 and 870.3 eV, respectively, along with their satellite peaks (marked as "sat.") at 860.20 and 877.5 eV, indicating the formation of the

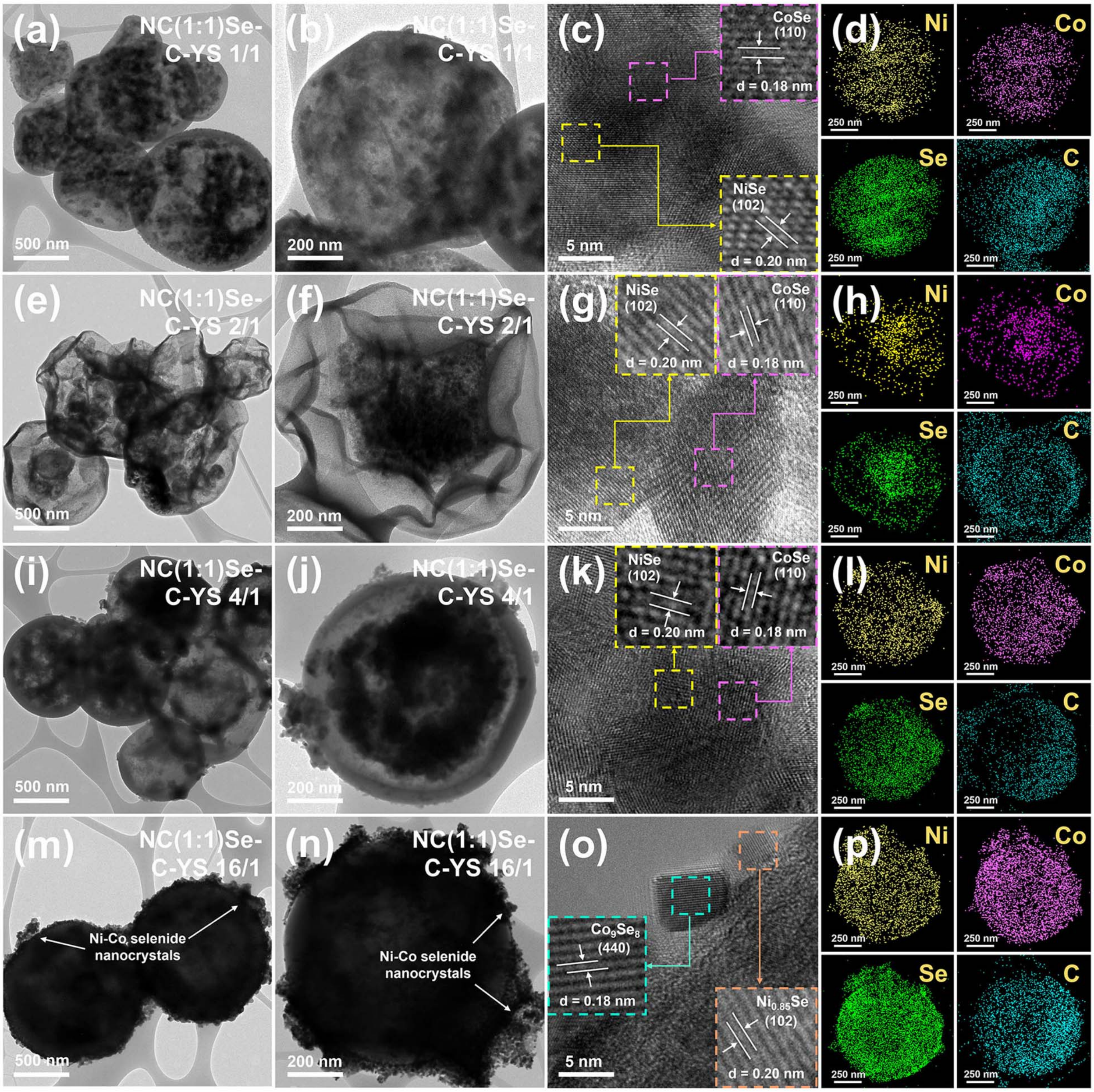

Fig. 3 TEM images, HR-TEM images, and elemental mapping of (a–d) NC(1 : 1)Se–C-YS 1/1, (e–h) NC(1 : 1)Se–C-YS 2/1, (i–l) NC(1 : 1)Se–C-YS 4/1, and (m–p) NC(1 : 1)Se–C-YS 16/1: (a, b, e, f, i, j, m, and n) TEM images, (c, g, k, and o) HR-TEM images, and (d, h, l, and p) elemental mapping.

NiSe phase.[38,39] Four additional peaks at binding energies of 855.4, 862.1, 873.1, and 879.99 eV were assigned to the nickel selenite phase formed from the partial oxidation of the nickel selenide surface. The Co 2p spectrum in Fig. 4c showed a similar fitting to the Ni 2p spectrum, with $Co_{3/2}$ and $Co_{1/2}$ peaks at 777.9 and 793.1 eV, respectively, and their satellite peaks (marked as "sat.") at 783.9 and 801.0 eV, indicating the formation of the CoSe phase. Additionally, four peaks corresponding to cobalt selenite phases were observed.[40,41] The Se 3d spectrum in Fig. 4d displayed Se $3d_{3/2}$ and Se $3d_{5/2}$ peaks at 54.7 and 53.8 eV, respectively, confirming the presence of the nickel–cobalt selenide phase. Three additional peaks at 58.7, 59.9, and 60.4 eV were assigned to partially oxidized metal selenite phases.[42–44] As confirmed by the elemental mapping image in Fig. S6,† the N 1s spectrum originating from N-doped carbon formed by the decomposition of PVP (Fig. 4e) was deconvoluted into three peaks at 398.2, 399.6, and 401.3 eV, representing pyridinic N, pyrrolic N, and graphitic N, respectively.[45–47] The XPS C 1s spectra and Raman spectra were analyzed to characterize the carbon components in NC(1 : 1)Se–C-YS 2/1, as shown in Fig. 4f and g, respectively. The high-resolution XPS C 1s spectra exhibited three deconvoluted peaks at 284.3, 285.3, and 288.5 eV, corresponding to C–C/C═C, C–N, and C═O bonds, respectively.[48] The Raman spectra in Fig. 4g reflected the results of the XPS C 1s spectra, with separate D (1346.1 cm^{-1}) and G (1597.2 cm^{-1}) bands, attributed to defective carbon and

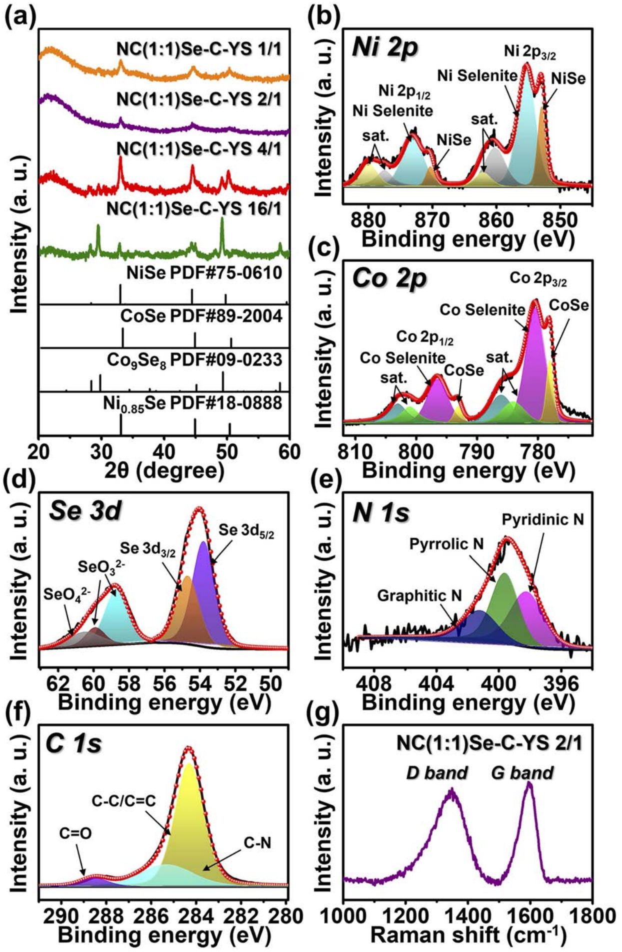

Fig. 4 (a) XRD patterns of nickel–cobalt selenide–carbon yolk–shell composites. XPS spectra and Raman spectra of NC(1 : 1)Se–C–YS 2/1: (b) Ni 2p spectrum, (c) Co 2p spectrum, (d) Se 3d spectrum, (e) N 1s spectrum, (f) C 1s spectrum, and (g) Raman spectrum.

graphitic carbon, respectively.[49–51] The Raman spectra of NC(1 : 1)Se–C-YS 1/1, NC(1 : 1)Se–C-YS 4/1, and NC(1 : 1)Se–C-YS 16/1 in Fig. S9† exhibited similar carbon properties. The thermogravimetric (TG) curves of the four samples are shown in Fig. S10.† All four samples showed a rapid weight loss between 400 and 500 °C, indicating the decomposition of nickel–cobalt selenide into nickel–cobalt oxide and carbon combustion. The weight loss of NC(1 : 1)Se–C-YS 1/1, NC(1 : 1)Se–C-YS 2/1, NC(1 : 1)Se–C-YS 4/1, and NC(1 : 1)Se–C-YS 16/1 were 63.7, 67.4, 58.5, and 60.8 wt%, respectively. The carbon content of NC(1 : 1)Se–C-YS 2/1 was estimated from the TG result to be 45.2 wt%. Additionally, owing to the synthesis process where the samples are infiltrated with a solution containing 1.75 g of nickel nitrate and 1.75 g of cobalt nitrate per 1 g of carbon yolk–shell, the carbon contents of NC(1 : 1)Se–C-YS 1/1, NC(1 : 1)Se–C-YS 4/1, and NC(1 : 1)Se–C-YS 16/1 are estimated to be similar to that of NC(1 : 1)Se–C-YS 2/1.[52]

The electrochemical properties of various samples with different shell thicknesses of yolk–shell structured nickel–cobalt selenide–carbon composite microspheres were systematically compared using diverse measurements. Cyclic voltammetry (CV) testing was conducted for four electrodes ranging from NC(1 : 1)Se–C-YS 1/1 to NC(1 : 1)Se–C-YS 16/1 within a potential range of 0.001–3.0 V (*versus* Na^+/Na) during the initial 5 cycles at a scan rate of 0.1 mV s^{-1}, as shown in Fig. 5. During the initial cathodic sweep, all four electrodes exhibited two obvious peaks at around 0.71 and 0.35 V. The first peak at 0.71 V was related to the reduction of nickel–cobalt selenide into metallic Ni, Co, and Na_2Se, as well as the formation of solid electrolyte interphase (SEI) layers.[53,54] Interestingly, NC(1 : 1)Se–C-YS 16/1 showed an additional sharp reduction peak at 0.66 V, which can be attributed to the conversion reduction reaction of $Ni_{0.85}Se$ and Co_9Se_8. The second reduction peak at 0.35 V could be associated with sodium ion intercalation into soft or hard carbon, which is derived from the decomposition of PVP and sucrose, respectively.[55] NC(1 : 1)Se–C-YS 1/1 represented a small reduction peak at 0.83 V compared to the other electrodes. This is likely due to the deep infiltration of the nickel–cobalt salt dissolved solution inside the yolk-carbon part, resulting in the formation of small nickel–cobalt selenide nanocrystals in the deep yolk carbon. In the subsequent anodic sweep, the sharp peak at around 1.83 V corresponded to the restitution and splitting of the nickel selenide and cobalt selenide nanocrystals.[56,57] After the second cycle, all four electrodes formed heterointerfaced nickel selenide and cobalt selenide nanocomposites, and they showed the same reduction (0.98 V) and oxidation (1.84 V) peaks. Additionally, CV testing for C-YS 1/1, C-YS 2/1, C-YS 4/1, and C-YS 16/1 electrodes was conducted within a potential range of 0.001–3.0 V (*versus* Na^+/Na) during the initial 5 cycles at a scan rate of 0.1 mV s^{-1}, as shown in Fig. S11.† During the initial cathodic sweep, all four C-YS electrodes were observed at 1.05 V and 0.75 V. These peaks are attributed to the irreversible reaction of the functional groups on the carbon surface with the electrolyte.[58] The sharp peak at 0.01 V is related to the intercalation of sodium ions into carbon.[59]

To evaluate the resistance and sodium ion diffusion behavior during charging and discharging of the electrodes, considering the shell thickness and the position of active

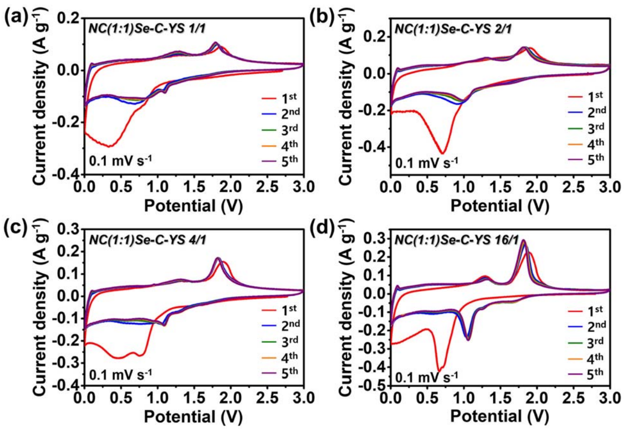

Fig. 5 CV curves of (a) NC(1 : 1)Se–C–YS 1/1, (b) NC(1 : 1)Se–C–YS 2/1, (c) NC(1 : 1)Se–C–YS 4/1, and (d) NC(1 : 1)Se–C–YS 16/1 at a scan rate of 0.1 mV s^{-1}.

nanocrystals within the yolk–shell structure, we performed *in situ* electrochemical impedance spectroscopy (EIS) at preselected potentials during the initial discharging and charging process, as depicted in Fig. 6a–l. The Nyquist plots of the four electrodes, ranging from NC(1 : 1)Se–C-YS 1/1 to NC(1 : 1)Se–C-YS 16/1, obtained through *in situ* EIS measurements during the initial cycle, are presented in Fig. 6a–d. In this study, we defined R_{tot} as the sum of interfacial resistance and charge transfer resistance, and the R_{tot} *vs.* potential graphs revealed different resistance variations during the first cycle, as shown in Fig. 6e–h. The four electrodes demonstrated similar R_{tot} value change behavior during the initial cycle. Initially, R_{tot} exhibited a relatively larger value until 0.8 V, which could be attributed to the aging of Na-ions that initiated the sodiation process. The rapid decrease in the R_{tot} value sat. around 1.0 V was related to the reduction of nickel–cobalt selenide into ultrafine metallic Ni and Co nanocrystals with Na_2Se *via* an electrochemical conversion reaction.[60] Subsequently, the maintenance of the resistance value until the end of the discharge was related to the formation of SEI layers without electrical conductivity.[61] During the charging process, the desodiation and partial dissolution of the SEI layer, ascribed to the electrocatalytic effect of metallic Ni and Co, contributed to a steady resistance reduction until around 1.8 V.[62] The drastic decrease in the R_{tot} value at 1.8 V

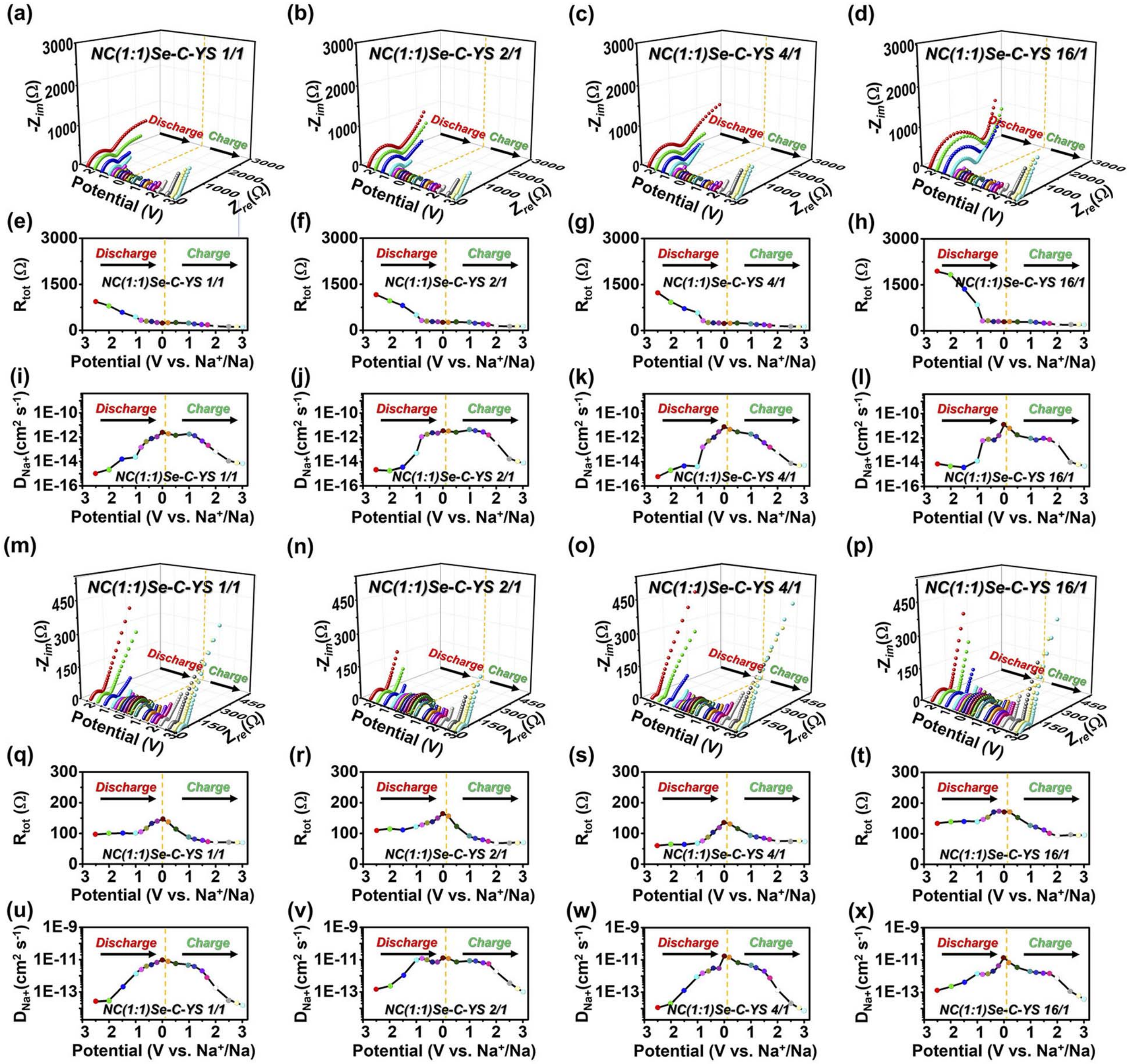

Fig. 6 (a–d) *In situ* EIS Nyquist plots of NC(1 : 1)Se–C-YS 1/1, NC(1 : 1)Se–C-YS 2/1, NC(1 : 1)Se–C-YS 4/1, and NC(1 : 1)Se–C-YS 16/1 measured at preselected potentials during the first cycle, (e–h) *in situ* EIS graphs (R_{tot} *vs.* potential), and (i–l) variations in sodium-ion diffusion coefficients calculated from the *in situ* EIS results. (m–p) *In situ* EIS Nyquist plots of NC(1 : 1)Se–C-YS 1/1, NC(1 : 1)Se–C-YS 2/1, NC(1 : 1)Se–C-YS 4/1, and NC(1 : 1)Se–C-YS 16/1 measured at preselected potentials after 100 cycles, (q–t) *in situ* EIS graphs (R_{tot} *vs.* potential), and (u–x) variations in sodium-ion diffusion coefficients calculated from the *in situ* EIS results.

might be attributed to the formation of the heterointerfaced nickel selenide–cobalt selenide nanocomposite, which exhibited improved electrical conductivity.[63,64] Among the three electrodes (NC(1 : 1)Se–C-YS 1/1, NC(1 : 1)Se–C-YS 2/1, and NC(1 : 1)Se–C-YS 4/1) that showed analogous R_{tot} values, NC(1 : 1)Se–C-YS 16/1 exhibited larger R_{tot} values. This could be attributed to the fact that the nickel–cobalt selenide nanocrystals, which did not penetrate deeply into the interior, formed large crystals on the surface due to the thick carbon shell, leading to the formation of a thick SEI and low reactivity on the surface. Furthermore, we calculated the variations in the sodium ion diffusion coefficient ($D_{\mathrm{Na^+}}$) of the four electrodes from the *in situ* EIS results. The diffusion coefficient of Na-ions can be determined using the following equation:

$$D_{\mathrm{Na^+}} = 0.5(RT/Sn^2F^2C\sigma)^2$$

A description of parameter values from previous studies has been provided.[44,65] During the initial discharging process, the variation in sodium ion diffusion showed a trend opposite to that of the total resistance, as depicted in Fig. 6i–l. The sharp increase in $D_{\mathrm{Na^+}}$ at around 0.8 V was attributed to the transformation of relatively large nickel–cobalt selenide nanocrystals into ultrafine metallic Ni and Co nanocrystals, leading to fast sodium ion diffusion.[42,66] Conversely, the desodiation process exhibited similar decreasing trends. The heterointerfaces of nickel selenide and cobalt selenide nanocomposites contributed to improved electrical conductivity but acted as a barrier to the diffusion of sodium ions. Additionally, the increase in crystal size from ultrafine nanocrystals to nickel selenide–cobalt selenide affected the decrease in the diffusion rate of sodium ions. After repeated 100 cycles, we compared the resistance and sodium ion diffusion behavior of the electrodes, as shown in Fig. 6m–x. During the discharging and charging process in the 100th cycle, the variation in resistances of the four electrodes exhibited similar trends. The large change in resistance value in the low potential range indicated that the process of intercalation and deintercalation of sodium ions into the carbon component, rather than nickel selenide and cobalt selenide nanocrystals, was the primary factor affecting the cycles. In the 100th cycle, nickel selenide and cobalt selenide nanocrystals were charged and discharged in a state where they were divided into very small sizes. Upon recharge after the 100th cycle, the NC(1 : 1)Se–C-YS 2/1 electrode showed the smallest resistance value. This result verified that the NC(1 : 1)Se–C-YS 2/1 sample has an optimized carbon shell thickness, as well as nanocrystal size and distribution. Additionally, the comparison of the diffusion rate of sodium ions also showed that the NC(1 : 1)Se–C-YS 2/1 electrode maintained the fastest rate on average.

The galvanostatic intermittent titration technique (GITT) analysis was conducted to compare the chemical diffusion coefficient. The GITT potential profiles of the four electrodes at the initial stage and after 100 cycles are shown in Fig. 7. The $D_{\mathrm{Na^+}}$ can be obtained using the following equation:

$$D_{\mathrm{Na^+}} = 4/\pi\tau(m_{\mathrm{B}}V_{\mathrm{M}}/M_{\mathrm{B}}S)^2(\Delta E_{\mathrm{s}}/\Delta E_{\tau})^2$$

The relevant parameter values have been documented in previous studies.[67–69] When comparing the sodium ion diffusion behavior observed in the *in situ* EIS measurement in Fig. 6, a clearer change is apparent from the GITT results. During the initial cycle, all four electrodes exhibited a similar variation of $D_{\mathrm{Na^+}}$. The significant decrease in $D_{\mathrm{Na^+}}$ at around 1.0 V during the initial sodiation can be attributed to the volume expansion of the electrode, and the subsequent increase in $D_{\mathrm{Na^+}}$ after 1.0 V is linked to the transformation of relatively large nickel–cobalt selenide nanocrystals into ultrafine metallic Ni and Co nanocrystals. Conversely, the decrease in the $D_{\mathrm{Na^+}}$ value at around 2.0 V during the initial desodiation can be attributed to the formation of heterointerfaces between nickel selenide and cobalt selenide nanocomposites, as confirmed in Fig. 6. Both during the initial cycle and after 100 cycles, the NC(1 : 1)Se–C-YS 2/1 electrode consistently exhibited relatively higher $D_{\mathrm{Na^+}}$ values compared to the other electrodes, indicating an optimized thickness of the carbon shell, as well as an optimal size and distribution of nanocrystals in the yolk–shell structure. However, it is worth noting that the $D_{\mathrm{Na^+}}$ values calculated from GITT and EIS measurements showed a similar trend of variation but exhibited quite different absolute values. This discrepancy is likely due to inherent uncertainties in both techniques, as reported in the previous literature.[70]

To determine the optimal ratio of Ni and Co, infiltration by varying the ratio of nickel nitrate hexahydrate and cobalt nitrate hexahydrate was conducted and nickel–cobalt selenide–carbon yolk–shell according to the ratio of nickel and cobalt was obtained. The SEM images of the four samples (NC(1 : 0)Se–C-YS 2/1, NC(2 : 1)Se–C-YS 2/1, NC(1 : 2)Se–C-YS 2/1, and NC(0 : 1)Se–C-YS 2/1) in Fig. S14† revealed similar SEM images corresponding to NC(1 : 1)Se–C-YS 2/1 (Fig. S4†). The XRD data of the four nickel–cobalt selenide–carbon yolk–shell microspheres with different ratios of Ni and Co in Fig. S15† showed that NC(1 : 0)Se–C-YS 2/1 exhibited the NiSe (PDF #75-0610) phase, while NC(0 : 1)Se–C-YS 2/1 showed the CoSe (PDF #89-2004) phase. Similarly to NC(1 : 1)Se–C-YS 2/1, both NC(2 : 1)Se–C-YS 2/1 and NC(1 : 2)Se–C-YS 2/1 displayed a slight shift in their XRD patterns due to the formation of NiSe and CoSe solid-solution. In the case of NC(1 : 2)Se–C-YS 2/1, $\mathrm{Ni_{0.85}Se}$ and $\mathrm{Co_9Se_8}$ phases are slightly observed. The electrochemical performances of the four samples (NC(1 : 0)Se–C-YS 2/1, NC(2 : 1)Se–C-YS 2/1, NC(1 : 2)Se–C-YS 2/1, and NC(0 : 1)Se–C-YS 2/1) according to the molar ratio of Ni and Co as anodes for sodium-ion batteries were evaluated as shown in Fig. S16.† The cycling performances of the four electrodes at a current density of 1 A g^{-1} after the initial 5 cycles at 0.1 A g^{-1} are investigated. Overall, similar cycle stability is shown depending on the ratio of Ni and Co. This revealed that the nickel–cobalt selenide nanocrystals, which were uniformly embedded within the carbon yolk–shell microsphere, facilitated the structural stability of the material as confirmed in the SEM images. However, rate performance evaluation showed a clear difference in properties depending on the ratio of Ni and Co. In general, it was known that multi-component compositions maintained a small crystal size by reducing agglomeration of crystals during

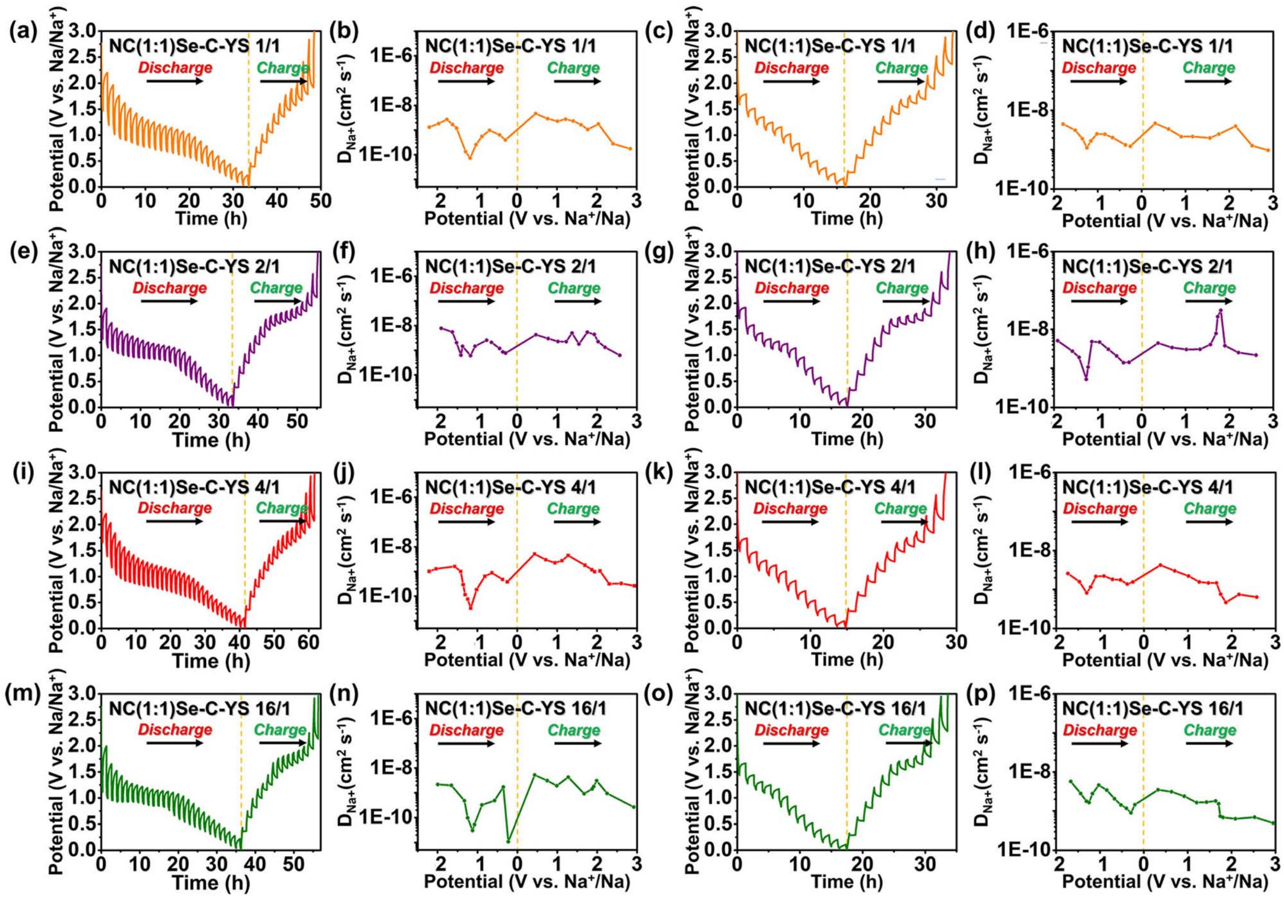

Fig. 7 (a, e, i and m) Galvanostatic intermittent titration technique (GITT) potential profiles during the initial cycle and (b, f, j and n) sodium-ion diffusion coefficients calculated from the GITT results. (c, g, k and o) GITT potential profiles after 100 cycles, and (d, h, l and p) sodium-ion diffusion coefficients calculated from the GITT results. (a–d) NC(1 : 1)Se–C-YS 1/1, (e–h) NC(1 : 1)Se–C-YS 2/1, (i–l) NC(1 : 1)Se–C-YS 4/1, and (m–p) NC(1 : 1)Se–C-YS 16/1.

conversion reactions of the charge and discharge process compared to single-component compositions. It could act most effectively in the multi-component phase of nickel–cobalt selenide compared to the single phases of NiSe and CoSe, and this is confirmed in the rate characteristic results. As a result, when Ni and Co are 1 : 1, they most effectively alleviate each other's crystal growth and show the best rate characteristics, so in this study, the ratio of Ni and Co was decided to be 1 : 1. The initial discharge and charge curves of the four electrodes at a current density of 0.2 A g^{-1} are shown in Fig. 8a. The prominent plateaus at 0.71 and 1.83 V during discharging and charging processes correspond to the cathodic and anodic peaks observed in the CV curves (Fig. 5). In the case of NC(1 : 1)Se–C-YS 16/1, the plateau during the initial sodiation is at a relatively low potential, which corresponds to the conversion reduction reaction of $Ni_{0.85}Se$ and Co_9Se_8, as confirmed in Fig. 5d. The initial discharge capacities of NC(1 : 1)Se–C-YS 1/1, NC(1 : 1)Se–C-YS 2/1, NC(1 : 1)Se–C-YS 4/1, and NC(1 : 1)Se–C-YS 16/1 were 928.3, 874.7, 908.7, and 730.1 mA h g^{-1}, respectively, with corresponding initial coulombic efficiencies of 40, 53, 46, and 50%, respectively. Notably, the NC(1 : 1)Se–C-YS 2/1 electrode displayed the highest initial coulombic efficiency, indicating that its carbon shell thickness, crystal distribution, and size were optimized for sodium ion storage properties. The cycling performances

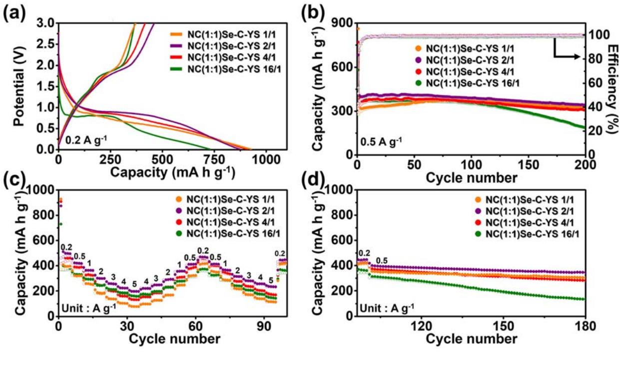

Fig. 8 Electrochemical properties of NC(1 : 1)Se–C-YS 1/1, NC(1 : 1)Se–C-YS 2/1, NC(1 : 1)Se–C-YS 4/1, and NC(1 : 1)Se–C-YS 16/1 electrodes: (a) initial discharge and charge curves, (b) cycle performances at a current density of 0.5 A g^{-1}, (c) triplicate evaluations of rate performances from 0.2 to 5 A g^{-1} and (d) cycle performances after repeated rate evaluation.

of the four electrodes at a current density of 0.5 A g^{-1} are presented in Fig. 8b. NC(1 : 1)Se–C-YS 1/1 exhibited a low capacity at the beginning, which gradually increased up to the initial 100 cycles. This behavior can be attributed to the location of nickel–cobalt selenide nanocrystals deep inside the yolk part, resulting in low initial capacities. However, the gradual breaking of the yolk part during cycling led to an increase in capacity. After 100 cycles, a decrease in capacity was observed due to structural instability caused by thin shell thickness. In contrast, the NC(1 : 1)Se–C-YS 16/1 electrode showed low and continuous decay of capacities during the 200 cycles, which was attributed to the thick carbon shell and the exposed crystal-grown nickel–cobalt selenide on the surface, leading to electrochemical structural instability. On the other hand, NC(1 : 1)Se–C-YS 2/1 showed stable cycling characteristics while maintaining a higher capacity compared to NC(1 : 1)Se–C-YS 4/1. The discharge capacities of NC(1 : 1)Se–C-YS 1/1, NC(1 : 1)Se–C-YS 2/1, NC(1 : 1)Se–C-YS 4/1, and NC(1 : 1)Se–C-YS 16/1 for the 200th cycle were 327.5, 342.4, 308.2, and 186.6 mA h g^{-1}, respectively, and their capacity retentions measured from the 2nd cycle were 98, 84, 80, and 47%, respectively. These results demonstrate the favorable cycling stability and capacity retention of NC(1 : 1)Se–C-YS 2/1, indicating the effectiveness of its optimized structural parameters. The rate performances of the four electrodes are shown in Fig. 8c. In this measurement, the current density was evaluated in triplicate from 0.2 to 5 A g^{-1}. As the rate was increased up to the 35th cycle, NC(1 : 1)Se–C-YS 2/1 demonstrated superior rate capabilities compared to NC(1 : 1)Se–C-YS 1/1, even though their cycle characteristics were similar, as shown in Fig. 8b. This finding indicates that the optimized thickness of the shell in NC(1 : 1)Se–C-YS 2/1, along with the distribution and size of the nanocrystals, exhibited excellent rate characteristics at high current densities. Conversely, NC(1 : 1)Se–C-YS 1/1 exhibited the lowest rate capabilities during the repeated rate evaluation due to its structural instability with a thin carbon shell. Specifically, NC(1 : 1)Se–C-YS 2/1 showed reversible discharge capacities of 500.2, 422.3, 365.7, 300.7, 260.0, 225.9, and 198.5 mA h g^{-1} at current densities of 0.2, 0.5, 1, 2, 3, 4, and 5 A g^{-1}, respectively. This performance is an improvement over those of previously reported nickel–cobalt selenide–carbon composite anode materials for sodium-ion batteries (Table S2†). After 35 cycles of repeated rate evaluation, NC(1 : 1)Se–C-YS 2/1 continued to exhibit the best rate capabilities. The cycle performances of the four electrodes after repeated rate evaluations are shown in Fig. 8d. NC(1 : 1)Se–C-YS 2/1 also displayed stable reversible capacities at a current density of 0.5 A g^{-1} after repeated cycling at high current densities. The SEM images in Fig. S13† show that the cycled NC(1 : 1)Se–C-YS 1/1, NC(1 : 1)Se–C-YS 2/1, and NC(1 : 1)Se–C-YS 4/1 electrodes exhibit similar stability without any structural breaking. However, the NC(1 : 1)Se–C-YS 16/1 electrode displays severe structural degradation owing to its thick shells and exposed nickel–cobalt selenide crystals. In addition, XRD analyses on the NC(1 : 1)Se–C-YS 1/1, NC(1 : 1)Se–C-YS 2/1, NC(1 : 1)Se–C-YS 4/1, and NC(1 : 1)Se–C-YS 16/1 microspheres at a fully charged state after stability tests were performed to demonstrate stability of the electrode materials. All NC(1 : 1)Se–C-YS electrodes after cyclic testing demonstrate a nearly amorphous crystalline characteristic as shown in Fig. S12.† During the discharging process, the nickel–cobalt selenide anode transformed into the ultrafine Ni nanocrystals and Co nanocrystals dispersed within the Na_2Se matrix. Additionally, the formation of an SEI layer, primarily composed of Na_2CO_3 and NaF, was observed. These species from the discharging process exhibited low crystallinity. During the charging process, the previously discharged species (metallic Ni, Co and Na_2Se) transformed into the NiSe and CoSe phases through the reverse conversion reaction. The species from the charging process also exhibited low crystallinity, making them challenging to detect by XRD. However, the corresponding peaks, which are related to the SEI layer in NC(1 : 1)Se–C-YS 2/1 showed the lowest crystallinity, indicating that the thinnest and most stable SEI layer was formed. A stable SEI layer could affect the cycling stability of the anode material for sodium ion batteries.[71,72] To demonstrate the effect of improving electrochemical properties with the carbon component, a nickel–cobalt selenide–yolk–shell without a carbon component was prepared through selenization from nickel–cobalt oxide yolk–shell, which was produced by oxidation of nickel–cobalt salt infiltrated carbon yolk–shell. The SEM images and XRD patterns in Fig. S17 and S18† confirm its yolk–shell structure and the formation of $(Ni_{0.5}Co_{0.5})Se$, $Ni_{0.85}Se$, and Co_9Se_8 composites. The CV curves in Fig. S19a† exhibited only one distinct peak related to the reduction conversion reaction of nickel–cobalt selenide near 0.67 V, with no peak for carbon intercalation of sodium ions near 0.44 V. The initial discharge and charge curves in Fig. S19b† showed higher initial coulombic efficiencies compared to those of NC(1 : 1)Se–C-YS electrodes, indicating that the carbon component influenced the initial irreversibility. The cycle performance and rate properties in Fig. S19c and d† demonstrate that the carbon component plays a crucial role in the structural stability of the electrode during repeated cycling and contributes to its excellent rate properties at high current densities.

To gain insights into the reaction kinetics responsible for the excellent Na-ion storage performance of NC(1 : 1)Se–C-YS 2/1, CV-rate measurements were conducted at various scan rates of 0.1, 0.2, 0.4, 0.6, 0.8, 1.0, 1.5, and 2.0 mV s^{-1}, spanning the potential range of 0.001–3 V, as shown in Fig. 9. In the CV curves depicted in Fig. 9a, e, i and m, the intensities of the cathodic and anodic peaks exhibited an increasing trend with an increase in the scan rate, while also demonstrating slight shifts due to electrode polarization. Notably, NC(1 : 1)Se–C-YS 2/1 exhibited a relatively smaller shift compared to the other electrodes, indicating its superior reversibility. The relationship between the scan rate (v) and the measured peak current (i) was typically described using the following equation:

$$\log(i) = b\log(v) + \log(a)$$

The equation used to determine the b values is given as follows, where i represents the measured current and v denotes

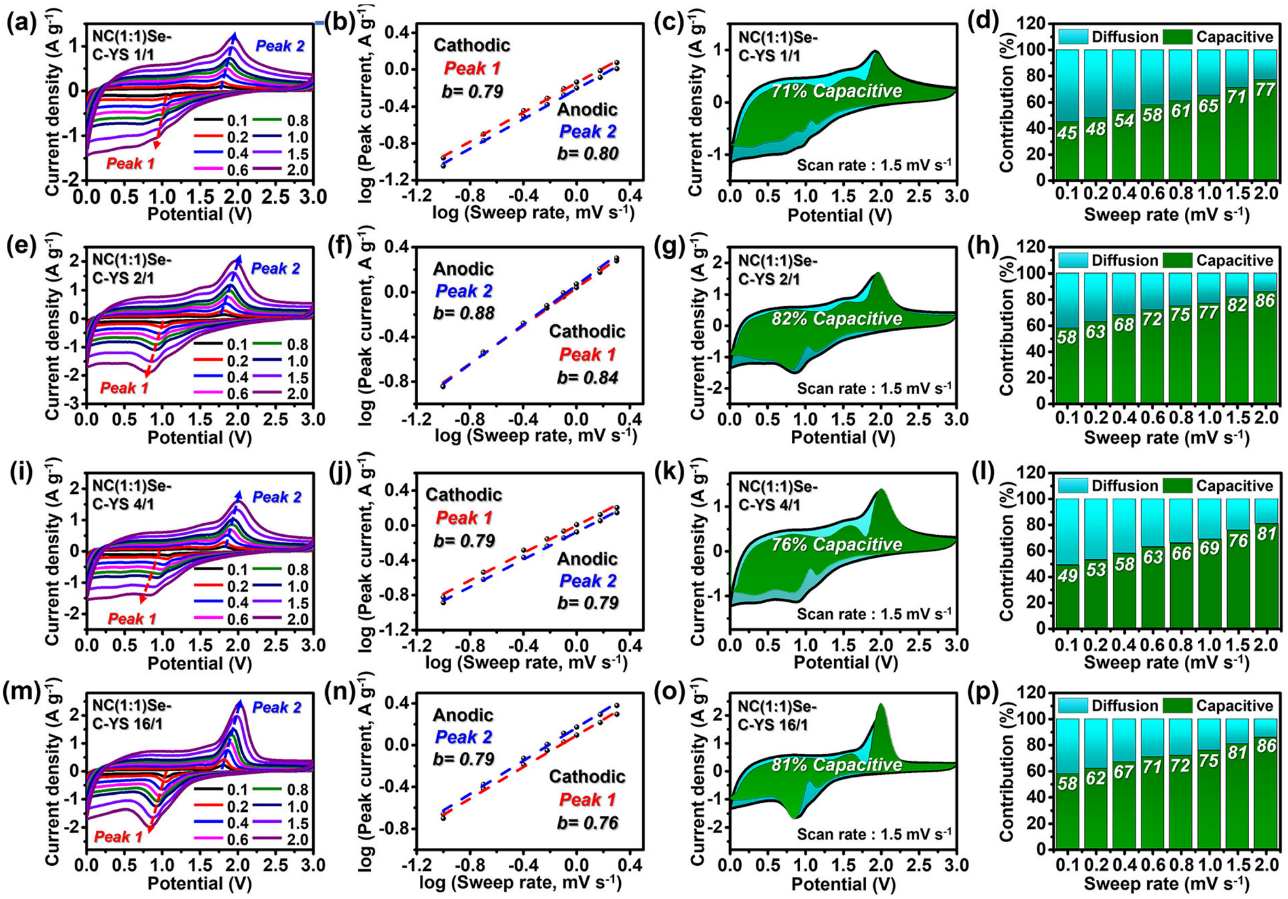

Fig. 9 (a, e, i and m) CV curves of the four electrodes at various scan rates, (b, f, j and n) fitted log(peak current) *vs.* log(scan rate) for peak 1 and peak 2, (c, g, k and o) CV curves showing capacitive contribution (green colored area) to the total current, and (d, h, l and p) capacity contribution at different scan rates. (a–d) NC(1 : 1)Se–C-YS 1/1, (e–h) NC(1 : 1)Se–C-YS 2/1, (i–l) NC(1 : 1)Se–C-YS 4/1, and (m–p) NC(1 : 1)Se–C-YS 16/1.

the scan rate.[73–76] A *b* value of 0.5 corresponds to diffusion-controlled behavior, while a *b* value of 1 represents an ideal capacitive behavior. For NC(1 : 1)Se–C-YS 1/1, NC(1 : 1)Se–C-YS 2/1, NC(1 : 1)Se–C-YS 4/1, and NC(1 : 1)Se–C-YS 16/1, the *b* values for the cathodic/anodic peaks were determined to be 0.79/0.80, 0.84/0.88, 0.79/0.79, and 0.76/0.79, respectively, by plotting $\log i$ *versus* $\log \nu$, as depicted in Fig. 9b, f, j and n. The relatively high *b* values of NC(1 : 1)Se–C-YS 2/1 were attributed to the optimized thickness of the carbon shell and the size and distribution of nanocrystals in the yolk–shell structure. The total capacitive contribution at a given scan rate can be divided into the capacitor-like current ($k_1\nu$) and the diffusion-controlled fraction ($k_2\nu^{1/2}$) at a fixed potential (V) according to the following equation:

$$i(V) = k_1\nu + k_2\nu^{1/2}$$

At a scan rate of 1.5 mV s^{-1}, NC(1 : 1)Se–C-YS 2/1 exhibited the highest capacitive contribution value at 82% compared to the other three samples. Moreover, NC(1 : 1)Se–C-YS 2/1 consistently demonstrated the highest average capacitive contribution value across all scan rates. This result aligns with the rate capability evaluation shown in Fig. 8c, confirming that NC(1 : 1)Se–C-YS 2/1 possesses excellent rate characteristics.

4. Conclusion

In this pioneering study, we proposed a novel approach to synthesize nanostructured carbon yolk–shell microspheres while precisely controlling the shell thickness. This was achieved by adjusting the ratio of PVP/sucrose in the spray solution used for spray pyrolysis, leading to the formation of yolk–shell microspheres with diverse shell thicknesses. Additionally, the combination of a metal salt dissolved solution-infiltration method facilitated the incorporation of ultrafine nickel–cobalt selenide nanocrystals within the carbon yolk–shell structure. The resulting composite materials, with their optimized shell thickness and nanocrystal size of nickel–cobalt selenides, were employed as anode materials for sodium-ion batteries, demonstrating exceptional electrochemical properties. The carefully tailored carbon yolk–shell composites exhibited excellent performance in energy storage applications. Moreover, these synthesis strategies can be extended to produce yolk–shell microspheres containing various metal or nonmetal composites, each with an optimal shell thickness. This design approach holds great promise for potential applications requiring the unique features of yolk–shell structures.

Conflicts of interest

There are no conflicts to declare.

Acknowledgements

This work was supported by a National Research Foundation of Korea (NRF) grant funded by the Korea Government (MEST) (NRF-2022R1F1A1070886). This work was supported by the National Research Foundation of Korea (NRF) grant funded by the Korea Government (MSIT) (No. RS-2023-00217581).

Notes and references

1 W. Xiong, Z. Wang, J. Zhang, C. Shang, M. Yang, L. He and Z. Lu, Hierarchical ball-in-ball structured nitrogen-doped carbon microspheres as high performance anode for sodium-ion batteries, *Energy Storage Mater.*, 2017, **7**, 229–235.

2 Y. Zhao, Q. Fu, D. Wang, Q. Pang, Y. Gao, A. Missiul, R. Nemausat, A. Sarapulova, H. Ehrenberg and Y. Wei, Co_9S_8@carbon yolk-shell nanocages as a high performance direct conversion anode material for sodium ion batteries, *Energy Storage Mater.*, 2019, **18**, 51–58.

3 Z. Li, Y. Fang, J. Zhang and X. W. Lou, Necklace-like structures composed of Fe_3N@C yolk–shell particles as an advanced anode for sodium-ion batteries, *Adv. Mater.*, 2018, **30**(30), 1800525.

4 Z. Liu, T. Lu, T. Song, X.-Y. Yu, X. W. D. Lou and U. Paik, Structure-designed synthesis of FeS_2@C yolk–shell nanoboxes as a high-performance anode for sodium-ion batteries, *Energy Environ. Sci.*, 2017, **10**(7), 1576–1580.

5 G. K. Veerasubramani, Y. Subramanian, M.-S. Park, G. Nagaraju, B. Senthilkumar, Y.-S. Lee and D.-W. Kim, Enhanced storage ability by using a porous pyrrhotite@N-doped carbon yolk–shell structure as an advanced anode material for sodium-ion batteries, *J. Mater. Chem. A*, 2018, **6**(41), 20056–20068.

6 J. Liu, P. Kopold, C. Wu, P. A. van Aken, J. Maier and Y. Yu, Uniform yolk–shell Sn_4P_3@C nanospheres as high-capacity and cycle-stable anode materials for sodium-ion batteries, *Energy Environ. Sci.*, 2015, **8**(12), 3531–3538.

7 C. Wu, X. Tong, Y. Ai, D.-S. Liu, P. Yu, J. Wu and Z. M. Wang, A review: enhanced anodes of Li/Na-ion batteries based on yolk–shell structured nanomaterials, *Nano-Micro Lett.*, 2018, **10**, 1–18.

8 J. Liu, S. Z. Qiao, J. S. Chen, X. W. D. Lou, X. Xing and G. Q. M. Lu, Yolk/shell nanoparticles: new platforms for nanoreactors, drug delivery and lithium-ion batteries, *Chem. Commun.*, 2011, **47**(47), 12578–12591.

9 J. Li, Q. Liu, Y. Zhang, J. Jiang, H. B. Wu and X.-Y. Yu, Copper and carbon-incorporated yolk-shelled FeP spheres with enhanced sodium storage properties, *Chem. Eng. J.*, 2021, **421**, 127776.

10 G. D. Park, J. H. Hong, J.-K. Lee and Y. C. Kang, Yolk–shell-structured microspheres composed of N-doped-carbon-coated $NiMoO_4$ hollow nanospheres as superior performance anode materials for lithium-ion batteries, *Nanoscale*, 2019, **11**(2), 631–638.

11 J. Liu, L. Yu, C. Wu, Y. Wen, K. Yin, F.-K. Chiang, R. Hu, J. Liu, L. Sun and L. Gu, New nanoconfined galvanic replacement synthesis of hollow Sb@C yolk–shell spheres constituting a stable anode for high-rate Li/Na-ion batteries, *Nano Lett.*, 2017, **17**(3), 2034–2042.

12 C. Cui, X. Guo, Y. Geng, T. Dang, G. Xie, S. Chen and F. Zhao, Facile one-pot synthesis of multi-yolk–shell Bi@ C nanostructures by the nanoscale Kirkendall effect, *Chem. Commun.*, 2015, **51**(45), 9276–9279.

13 J.-S. Park, S. Y. Yang, J.-K. Lee and Y. C. Kang, A novel strategy for encapsulating metal sulfide nanoparticles inside hollow carbon nanosphere-aggregated microspheres for efficient potassium ion storage, *J. Mater. Chem. A*, 2022, **10**(34), 17790–17800.

14 H. Zhang, L. Zhou, O. Noonan, D. J. Martin, A. K. Whittaker and C. Yu, Tailoring the void size of iron oxide@carbon yolk–shell structure for optimized lithium storage, *Adv. Funct. Mater.*, 2014, **24**(27), 4337–4342.

15 Y.-A. Chen, Y.-T. Wang, H. S. Moon, K. Yong and Y.-J. Hsu, Yolk–shell nanostructures: synthesis, photocatalysis and interfacial charge dynamics, *RSC Adv.*, 2021, **11**(20), 12288–12305.

16 S. Chen, X. Huang, B. Sun, J. Zhang, H. Liu and G. Wang, Multi-shelled hollow carbon nanospheres for lithium–sulfur batteries with superior performances, *J. Mater. Chem. A*, 2014, **2**(38), 16199–16207.

17 Y. Zhao, X. Shi, S. J. H. Ong, Q. Yao, B. Chen, K. Hou, C. Liu, Z. J. Xu and L. Guan, Enhancing the charge transportation ability of yolk–shell structure for high-rate sodium and potassium storage, *ACS Nano*, 2020, **14**(4), 4463–4474.

18 H. Zhang, X. Huang, O. Noonan, L. Zhou and C. Yu, Tailored yolk–shell Sn@C nanoboxes for high-performance lithium storage, *Adv. Funct. Mater.*, 2017, **27**(8), 1606023.

19 Y. Wang, F. Zhang, Y. Yu, Y. Yang, P. Mao, W. Guo, S. Rao, D. Wang and Q. Li, Tailoring the carbon shell thickness of SnCo@nitrogen-doped carbon nanocages for optimized lithium storage, *Electrochim. Acta*, 2018, **282**, 799–806.

20 L. Xie, Z. Yang, J. Sun, H. Zhou, X. Chi, H. Chen, A. X. Li, Y. Yao and S. Chen, Bi_2Se_3/C nanocomposite as a new sodium-ion battery anode material, *Nano-Micro Lett.*, 2018, **10**, 1–9.

21 P. Wang, J. Huang, J. Zhang, L. Wang, P. Sun, Y. Yang and Z. Yao, Coupling hierarchical iron cobalt selenide arrays with N-doped carbon as advanced anodes for sodium ion storage, *J. Mater. Chem. A*, 2021, **9**(11), 7248–7256.

22 Z. Hao, X. Shi, Z. Yang, L. Li and S. L. Chou, Developing High-Performance Metal Selenides for Sodium-Ion Batteries, *Adv. Funct. Mater.*, 2022, **32**(51), 2208093.

23 Y. Gong, Y. Li, Y. Li, M. Liu, Y. Bai and C. Wu, Metal selenides anode materials for sodium ion batteries:

synthesis, modification, and application, *Small*, 2023, **19**(4), 2206194.

24 L. Xia, Z. Yang, B. Tang, F. Li, J. Wei and Z. Zhou, Carbon Nanofibers with Embedded Sb_2Se_3 Nanoparticles as Highly Reversible Anodes for Na-Ion Batteries, *Small*, 2021, **17**(4), 2006016.

25 Y. Fang, X.-Y. Yu and X. W. Lou, Formation of polypyrrole-coated Sb_2Se_3 microclips with enhanced sodium-storage properties, *Angew. Chem., Int. Ed.*, 2018, **57**(31), 9859–9863.

26 S. H. Yang, S.-K. Park and Y. C. Kang, MOF-derived $CoSe_2$@N-doped carbon matrix confined in hollow mesoporous carbon nanospheres as high-performance anodes for potassium-ion batteries, *Nano-Micro Lett.*, 2021, **13**, 1–15.

27 X. Hu, X. Liu, K. Chen, G. Wang and H. Wang, Core–shell MOF-derived N-doped yolk–shell carbon nanocages homogenously filled with ZnSe and $CoSe_2$ nanodots as excellent anode materials for lithium-and sodium-ion batteries, *J. Mater. Chem. A*, 2019, **7**(18), 11016–11037.

28 Y. Zhang, A. Pan, Y. Wang, X. Cao, Z. Zhou, T. Zhu, S. Liang and G. Cao, Self-templated synthesis of N-doped $CoSe_2$/C double-shelled dodecahedra for high-performance supercapacitors, *Energy Storage Mater.*, 2017, **8**, 28–34.

29 B. Fei, Z. Yao, D. Cai, J. Si, Q. Wang, Q. Chen, B. Sa, K. Peng and H. Zhan, Construction of sugar gourd-like yolk-shell Ni–Mo–Co–S nanocage arrays for high-performance alkaline battery, *Energy Storage Mater.*, 2020, **25**, 105–113.

30 S. H. Yang, G. D. Park, J. K. Kim and Y. C. Kang, New strategy to synthesize optimal cobalt diselenide@hollow mesoporous carbon nanospheres for highly efficient hydrogen evolution reaction, *Chem. Eng. J.*, 2021, **424**, 130341.

31 S. H. Yang, S. K. Park, G. D. Park, J. H. Lee and Y. C. Kang, Conversion reaction mechanism of ultrafine bimetallic Co-Fe selenides embedded in hollow mesoporous carbon nanospheres and their excellent K-ion storage performance, *Small*, 2020, **16**(33), 2002345.

32 P. Ge, S. Li, L. Xu, K. Zou, X. Gao, X. Cao, G. Zou, H. Hou and X. Ji, Hierarchical hollow-microsphere metal–selenide@carbon composites with rational surface engineering for advanced sodium storage, *Adv. Energy Mater.*, 2019, **9**(1), 1803035.

33 C. Dong, L. Wu, Y. He, Y. Zhou, X. Sun, W. Du, X. Sun, L. Xu and F. Jiang, Willow-leaf-like ZnSe@N-doped carbon nanoarchitecture as a stable and high-performance anode material for sodium-ion and potassium-ion batteries, *Small*, 2020, **16**(47), 2004580.

34 H. Liu, M. Jia, Q. Zhu, B. Cao, R. Chen, Y. Wang, F. Wu and B. Xu, 3D-0D graphene-Fe_3O_4 quantum dot hybrids as high-performance anode materials for sodium-ion batteries, *ACS Appl. Mater. Interfaces*, 2016, **8**(40), 26878–26885.

35 W. Zhong, M. Tao, W. Tang, W. Gao, T. Yang, Y. Zhang, R. Zhan, S.-J. Bao and M. Xu, MXene-derivative pompon-like $Na_2Ti_3O_7$@C anode material for advanced sodium ion batteries, *Chem. Eng. J.*, 2019, **378**, 122209.

36 X. Chen and Y. Zhang, The main problems and solutions in practical application of anode materials for sodium ion batteries and the latest research progress, *Int. J. Energy Res.*, 2021, **45**(7), 9753–9779.

37 J. Yang, X. Wang, W. Dai, X. Lian, X. Cui, W. Zhang, K. Zhang, M. Lin, R. Zou and K. P. Loh, From micropores to ultra-micropores inside hard carbon: toward enhanced capacity in room-/low-temperature sodium-ion storage, *Nano-Micro Lett.*, 2021, **13**, 1–14.

38 Z. Zou, X. Wang, J. Huang, Z. Wu and F. Gao, An Fe-doped nickel selenide nanorod/nanosheet hierarchical array for efficient overall water splitting, *J. Mater. Chem. A*, 2019, **7**(5), 2233–2241.

39 S. H. Oh and J. S. Cho, Hierarchical (Ni, Co)Se_2/CNT hybrid microspheres consisting of a porous yolk and embossed hollow thin shell for high-performance anodes in sodium-ion batteries, *J. Alloys Compd.*, 2019, **806**, 1029–1038.

40 Y.-L. Liu, C. Yan, G.-G. Wang, F. Li, Q. Kang, H.-Y. Zhang and J.-C. Han, Selenium-rich nickel cobalt bimetallic selenides with core–shell architecture enable superior hybrid energy storage devices, *Nanoscale*, 2020, **12**(6), 4040–4050.

41 H. Li, X. Qian, C. Zhu, X. Jiang, L. Shao and L. Hou, Template synthesis of $CoSe_2$/Co_3Se_4 nanotubes: tuning of their crystal structures for photovoltaics and hydrogen evolution in alkaline medium, *J. Mater. Chem. A*, 2017, **5**(9), 4513–4526.

42 S. H. Lim, G. D. Park, D. S. Jung, J.-H. Lee and Y. C. Kang, Towards an efficient anode material for Li-ion batteries: understanding the conversion mechanism of nickel hydroxy chloride with Li-ions, *J. Mater. Chem. A*, 2020, **8**(4), 1939–1946.

43 G. Suo, J. Zhang, D. Li, Q. Yu, W. A. Wang, M. He, L. Feng, X. Hou, Y. Yang and X. Ye, N-doped carbon/ultrathin 2D metallic cobalt selenide core/sheath flexible framework bridged by chemical bonds for high-performance potassium storage, *Chem. Eng. J.*, 2020, **388**, 124396.

44 Z. Ali, T. Tang, X. Huang, Y. Wang, M. Asif and Y. Hou, Cobalt selenide decorated carbon spheres for excellent cycling performance of sodium ion batteries, *Energy Storage Mater.*, 2018, **13**, 19–28.

45 C. Zhao, G. Liu, N. Sun, X. Zhang, G. Wang, Y. Zhang, H. Zhang and H. Zhao, Biomass-derived N-doped porous carbon as electrode materials for Zn-air battery powered capacitive deionization, *Chem. Eng. J.*, 2018, **334**, 1270–1280.

46 S. Sun, T. Xie, S. Tao, P. Sheng, Z. Han, B. Qian and X. Jiang, Formation of nitrogen-doped carbon-coated CoP nanoparticles embedded within graphene oxide for lithium-ion batteries anode, *Energy Technol.*, 2020, **8**(3), 1901089.

47 L.-B. Ren, W. Hua, Z.-D. Hou and J.-G. Wang, Rational construction of CoP@C hollow structure for ultrafast and stable sodium energy storage, *Rare Met.*, 2022, **41**(6), 1859–1869.

48 A. Ghosh, S. Ghosh, G. M. Seshadhri and S. Ramaprabhu, Green synthesis of nitrogen-doped self-assembled porous carbon-metal oxide composite towards energy and environmental applications, *Sci. Rep.*, 2019, **9**(1), 5187.

49 Y. B. Kim, H. Y. Seo, S. H. Kim, T. H. Kim, J. H. Choi, J. S. Cho, Y. C. Kang and G. D. Park, Controllable Synthesis of Carbon Yolk-Shell Microsphere and Application of Metal Compound–Carbon Yolk-Shell as Effective Anode Material for Alkali-Ion Batteries, *Small Methods*, 2023, **7**(3), 2201370.

50 X. Chen, J. Tian, P. Li, Y. Fang, Y. Fang, X. Liang, J. Feng, J. Dong, X. Ai, H. Yang and Y. Cao, An overall understanding of sodium storage behaviors in hard carbons by an "adsorption-intercalation/filling" hybrid mechanism, *Adv. Energy Mater.*, 2022, **12**(24), 2200886.

51 X. Chen, N. Sawut, K. Chen, H. Li, J. Zhang, Z. Wang, M. Yang, G. Tang, X. Ai, H. Yang, Y. Fang and Y. Cao, Filling carbon: a microstructure-engineered hard carbon for efficient alkali metal ion storage, *Energy Environ. Sci.*, 2023, **16**(9), 4041–4053.

52 G. D. Park and Y. C. Kang, One-pot synthesis of $CoSe_x$–rGO composite powders by spray pyrolysis and their application as anode material for sodium-ion batteries, *Chem.–Eur. J.*, 2016, **22**(12), 4140–4146.

53 X. Yang, J. Zhang, Z. Wang, H. Wang, C. Zhi, D. Y. Yu and A. L. Rogach, Carbon-supported nickel selenide hollow nanowires as advanced anode materials for sodium-ion batteries, *Small*, 2018, **14**(7), 1702669.

54 S.-K. Park, J. K. Kim and Y. C. Kang, Metal–organic framework-derived $CoSe_2$/(NiCo)Se_2 box-in-box hollow nanocubes with enhanced electrochemical properties for sodium-ion storage and hydrogen evolution, *J. Mater. Chem. A*, 2017, **5**(35), 18823–18830.

55 Z. Zhu, F. Liang, Z. Zhou, X. Zeng, D. Wang, P. Dong, J. Zhao, S. Sun, Y. Zhang and X. Li, Expanded biomass-derived hard carbon with ultra-stable performance in sodium-ion batteries, *J. Mater. Chem. A*, 2018, **6**(4), 1513–1522.

56 K.-H. Chen, K. N. Wood, E. Kazyak, W. S. LePage, A. L. Davis, A. J. Sanchez and N. P. Dasgupta, Dead lithium: mass transport effects on voltage, capacity, and failure of lithium metal anodes, *J. Mater. Chem. A*, 2017, **5**(23), 11671–11681.

57 J. Liu, Z. Leng, H. Dong, X. Xu, C. Lv, H. Wei, L. Yu, J. Yang and H. Geng, In situ interface engineering of NiSe with interlinked conductive networks for high energy density sodium-ion half/full batteries, *Inorg. Chem. Front.*, 2023, **10**, 4076–4086.

58 K.-L. Hong, L. Qie, R. Zeng, Z.-Q. Yi, W. Zhang, D. Wang, W. Yin, C. Wu, Q.-J. Fan and W.-X. Zhang, Biomass derived hard carbon used as a high performance anode material for sodium ion batteries, *J. Mater. Chem. A*, 2014, **2**(32), 12733–12738.

59 W. Chen, C. Chen, X. Xiong, P. Hu, Z. Hao and Y. Huang, Coordination of surface-induced reaction and intercalation: toward a high-performance carbon anode for sodium-ion batteries, *Adv. Sci.*, 2017, **4**(6), 1600500.

60 S. H. Yang, Y. J. Lee, H. Kang, S.-K. Park and Y. C. Kang, Carbon-coated three-dimensional MXene/iron selenide ball with core–shell structure for high-performance potassium-ion batteries, *Nano-Micro Lett.*, 2022, **14**, 1–17.

61 J. Zhang, J. Lin, Y. Zeng, Y. Zhang and H. Guo, Morphological and structural evolution of MnO@C anode and its application in lithium-ion capacitors, *ACS Appl. Energy Mater.*, 2019, **2**(11), 8345–8358.

62 G. D. Park, J.-S. Park, J. K. Kim and Y. C. Kang, Metal sulfoselenide solid solution embedded in porous hollow carbon nanospheres as effective anode material for potassium-ion batteries with long cycle life and enhanced rate performance, *Chem. Eng. J.*, 2022, **428**, 131051.

63 G. D. Park, J. S. Park, J. K. Kim and Y. C. Kang, Recent advances in heterostructured anode materials with multiple anions for advanced alkali-ion batteries, *Adv. Energy Mater.*, 2021, **11**(27), 2003058.

64 J. Zong, F. Wang, C. Nie, M. Zhao and S. Yang, Cobalt and oxygen double doping induced C@MoS_2–CoS_2–O@ C nanocomposites with an improved electronic structure and increased active sites as a high-performance anode for sodium-based dual-ion batteries, *J. Mater. Chem. A*, 2022, **10**(19), 10651–10661.

65 Z. Wang, K. Dong, D. Wang, S. Luo, X. Liu, Y. Liu, Q. Wang, Y. Zhang, A. Hao and C. He, Constructing N-Doped porous carbon confined FeSb alloy nanocomposite with Fe-NC coordination as a universal anode for advanced Na/K-ion batteries, *Chem. Eng. J.*, 2020, **384**, 123327.

66 S. Huang, M. Wang, P. Jia, B. Wang, J. Zhang and Y. Zhao, N-graphene motivated SnO_2@SnS_2 heterostructure quantum dots for high performance lithium/sodium storage, *Energy Storage Mater.*, 2019, **20**, 225–233.

67 Y. Huang, X. Li, J. Luo, K. Wang, Q. Zhang, Y. Qiu, S. Sun, S. Liu, J. Han and Y. Huang, Enhancing sodium-ion storage behaviors in $TiNb_2O_7$ by mechanical ball milling, *ACS Appl. Mater. Interfaces*, 2017, **9**(10), 8696–8703.

68 L. Tao, Y. Yang, H. Wang, Y. Zheng, H. Hao, W. Song, J. Shi, M. Huang and D. Mitlin, Sulfur-nitrogen rich carbon as stable high capacity potassium ion battery anode: performance and storage mechanisms, *Energy Storage Mater.*, 2020, **27**, 212–225.

69 J. Jiang, Y. Zhang, Y. An, L. Wu, Q. Zhu, H. Dou and X. Zhang, Engineering ultrathin MoS_2 nanosheets anchored on N-doped carbon microspheres with pseudocapacitive properties for high-performance lithium-ion capacitors, *Small Methods*, 2019, **3**(7), 1900081.

70 C. Deng and W. Lu, Consistent diffusivity measurement between galvanostatic intermittent titration technique and electrochemical impedance spectroscopy, *J. Power Sources*, 2020, **473**, 228613.

71 J. M. Lee, G. Singh, W. Cha, S. Kim, J. Yi, S.-J. Hwang and A. Vinu, Recent advances in developing hybrid materials for sodium-ion battery anodes, *ACS Energy Lett.*, 2020, **5**(6), 1939–1966.

72 P. Xue, N. Wang, Z. Fang, Z. Lu, X. Xu, L. Wang, Y. Du, X. Ren, Z. Bai and S. Dou, Rayleigh-instability-induced bismuth nanorod@nitrogen-doped carbon nanotubes as a long cycling and high rate anode for sodium-ion batteries, *Nano Lett.*, 2019, **19**(3), 1998–2004.

73 X. Hu, J. Jia, G. Wang, J. Chen, H. Zhan and Z. Wen, Reliable and general route to inverse opal structured nanohybrids of carbon-confined transition metal sulfides quantum dots for

high-performance sodium storage, *Adv. Energy Mater.*, 2018, **8**(25), 1801452.

74 D. M. Zhang, J. H. Jia, C. C. Yang and Q. Jiang, Fe_7Se_8 nanoparticles anchored on N-doped carbon nanofibers as high-rate anode for sodium-ion batteries, *Energy Storage Mater.*, 2020, **24**, 439–449.

75 S. Nie, L. Liu, M. Li, J. Liu, J. Xia, Y. Zhang and X. Wang, $Na_2Ti_3O_7$/C Nanofibers for High-Rate and Ultralong-Life Anodes in Sodium-Ion Batteries, *ChemElectroChem*, 2018, **5**(22), 3498–3505.

76 J. Tian, J. Li, Y. Zhang, X.-Y. Yu and Z. Hong, Carbon-coated $CoSe_2$ nanoparticles confined in N-doped carbon microboxes with enhanced sodium storage properties, *J. Mater. Chem. A*, 2019, **7**(37), 21404–21409.